Resonant inner-shell photofragmentation of adamantane (C10H16)

Smita Ganguly, Mathieu Gisselbrecht, Per Eng-Johnsson, Raimu Feifel, Sergio Díaz-Tendero, Eva Muchová, Aleksandar R Milosavljević, Patrick Rousseau, Sylvain Maclot

▶ **To cite this version:**

Smita Ganguly, Mathieu Gisselbrecht, Per Eng-Johnsson, Raimu Feifel, Sergio Díaz-Tendero, et al.. Resonant inner-shell photofragmentation of adamantane (C10H16). Molecules, 2023, 28 (14), pp.5510. 10.3390/molecules28145510 . hal-04165873

HAL Id: hal-04165873
https://hal.science/hal-04165873

Submitted on 19 Jul 2023

HAL is a multi-disciplinary open access archive for the deposit and dissemination of scientific research documents, whether they are published or not. The documents may come from teaching and research institutions in France or abroad, or from public or private research centers.

L'archive ouverte pluridisciplinaire **HAL**, est destinée au dépôt et à la diffusion de documents scientifiques de niveau recherche, publiés ou non, émanant des établissements d'enseignement et de recherche français ou étrangers, des laboratoires publics ou privés.

molecules

MDPI

Article

Resonant Inner-Shell Photofragmentation of Adamantane (C10H16)

Smita Ganguly [1], Mathieu Gisselbrecht [1,†], Per Eng-Johnsson [1], Raimund Feifel [2], Sergio Díaz-Tendero [3,4,5], Eva Muchová [6], Aleksandar R. Milosavljević [7,*], Patrick Rousseau [8] and Sylvain Maclot [2,9,†]

1 Department of Physics, Lund University, 22100 Lund, Sweden; smita_omkarnath.ganguly@sljus.lu.se (S.G.); mathieu.gisselbrecht@sljus.lu.se (M.G.); per.eng-johnsson@fysik.lth.se (P.E.-J.)
2 Department of Physics, University of Gothenburg, Origovagen 6 B, 41296 Gothenburg, Sweden; raimund.feifel@physics.gu.se (R.F.); sylvain.maclot@univ-lyon1.fr (S.M.)
3 Department of Chemistry, Universidad Autonoma de Madrid, 28049 Madrid, Spain; sergio.diaztendero@uam.es
4 Institute for Advanced Research in Chemistry (IAdChem), Universidad Autónoma de Madrid, 28049 Madrid, Spain
5 Condensed Matter Physics Center (IFIMAC), Universidad Autónoma de Madrid, 28049 Madrid, Spain
6 Department of Physical Chemistry, University of Chemistry and Technology, Technická 5, 166 28 Prague, Czech Republic; eva.muchova@vscht.cz
7 Synchrotron SOLEIL, L'Orme de Merisiers, Saint Aubin, BP48, 91192 Gif-sur-Yvette CEDEX, France
8 Normandie University, ENSICAEN, UNICAEN, CEA, CNRS, CIMAP, 14000 Caen, France; prousseau@ganil.fr
9 Institut Lumiere Matiere UMR 5306, Universite Claude Bernard Lyon 1, CNRS, Univ. Lyon, 69100 Villeurbanne, France
* Correspondence: aleksandar.milosavljevic@synchrotron-soleil.fr
† These authors contributed equally to this work.

Abstract: Adamantane, the smallest diamondoid molecule with a symmetrical cage, contains two distinct carbon sites, CH and CH_2. The ionization/excitation of the molecule leads to the cage opening and strong structural reorganization. While theoretical predictions suggest that the carbon site CH primarily causes the cage opening, the role of the other CH_2 site remains unclear. In this study, we used advanced experimental Auger electron–ion coincidence techniques and theoretical calculations to investigate the fragmentation dynamics of adamantane after resonant inner-shell photoexcitation. Our results demonstrate that some fragmentation channels exhibit site-sensitivity of the initial core–hole location, indicating that different carbon site excitations could lead to unique cage opening mechanisms.

Keywords: adamantane; inner-shell fragmentation; site-selectivity; AE–PICO/PIPICO coincidence

check for updates

Citation: Ganguly, S.; Gisselbrecht, M.; Eng-Johnsson, P.; Feifel, R.; Díaz-Tendero, S.; Muchová, E.; Milosavljević, A.R.; Rousseau, P.; Maclot, S. Resonant Inner-Shell Photofragmentation of Adamantane (C10H16). *Molecules* **2023**, *28*, 5510. https://doi.org/10.3390/molecules28145510

Academic Editor: Francisco Torrens

Received: 30 May 2023
Revised: 10 July 2023
Accepted: 17 July 2023
Published: 19 July 2023

Copyright: © 2023 by the authors. Licensee MDPI, Basel, Switzerland. This article is an open access article distributed under the terms and conditions of the Creative Commons Attribution (CC BY) license (https://creativecommons.org/licenses/by/4.0/).

1. Introduction

Synchrotron radiation allows resonant excitation of a specific atomic site in molecules. Numerous studies of fragmentation of core-excited molecules have found site-selective fragmentation [1–17] where bond breaking often occurs near the excited atomic sites. However, between the site-specific core excitation and the molecular fragmentation, there is one more step, wherein the system undergoes Auger decay. Auger decay results in a widely spread energy distribution of final states, and charge delocalization leading to different ionic fragmentation pathways. Therefore, coincidence experiments between the energy-resolved Auger electron and the fragment ions are necessary to investigate the mechanisms leading to site-specific fragmentation. We studied site-selective fragmentation of adamantane ($C_{10}H_{16}$), the smallest diamondoid molecule, using multiparticle Auger electron–ion coincidence spectroscopy and advanced theoretical calculations.

The adamantane molecule consists of a carbon cage formed by $C(sp^3)$–$C(sp^3)$ hybridized bonds and fully terminated by hydrogen atoms, with two distinct carbon sites:

methanetriyl CH and methylene CH_2 groups. Valence dissociative ionization of adamantane has been studied using VUV radiation [18], XUV femtosecond pulses [19,20], electron ionization [21,22], and other spectroscopic techniques [23,24]. These studies have shown that the molecule tends to dissociate through multiple parallel channels that begin with the opening of the carbon cage and hydrogen migration from the CH site. In general, the fragmentation pattern of adamantane depends on the ionizing radiation. This is mainly due to the different orbitals involved in the ionizing process and the amount of internal energy deposited in the system. In our previous work [25], we found indirect evidence of site-sensitive fragmentation of adamantane after core-ionization of either the CH or CH_2 sites. Here, we extend our research to explore site-selective fragmentation of adamantane, using resonant excitation, and compare the results to the core ionization study.

In this work, we investigated the electronic relaxation of, and the subsequent fragmentation dynamics of. adamantane at the two resonant excitations [26,27] of C 1s → valence CH orbital and C 1s → valence CH_2 orbital at 287.1 eV and 287.6 eV, respectively. We modeled theoretical X-ray absorption spectra via single point and nuclear ensemble approaches to understand the nature of these excitations. We used theoretical calculations within the EOM–CCSD framework to interpret the measured resonant Auger electron spectra (RAES). Additionally, we predicted the nuclear dynamics in the core excited state of adamantane using the 'Z + 1 approximation'. We find clear site-dependent bond dissociation for the dominant fragmentation channels of the adamantane cation, proving site sensitivity to the initial core–hole localization, either on the CH or CH_2 carbon site. Interestingly, we noticed a significant decrease in the production of methylium (CH_3^+) when core-excited adamantane was compared to core-ionized adamantane. This finding suggests the existence of new mechanisms for cage-opening processes that do not involve hydrogen migration or CH_3 termination.

2. Results and Discussion

2.1. Resonant Excitation of Adamantane

Figure 1a presents the experimental total ion yield (TIY) and the theoretical XAS spectrum of adamantane below the C 1s ionization edge. We observed two sharp peaks at 287.1 eV and 287.6 eV, previously reported by Willey et al. [26,27], and assigned to C 1s → valence CH orbital and C 1s → valence CH_2 orbital transitions respectively. The theoretical XAS spectra were calculated at the CVS-EOM-EE-CCSD/6-31g* level, via the single point approach, and CAM-B3LYP/6-31g*, via the NEA approach. Both the theoretical XAS spectra were congruent with the experimental TIY spectral shape and spacing between the first and second peaks (other levels of theory and discussions are available in the Supplementary Materials). The experimental spectrum exhibited vibronic structures that were neglected in the calculations. According to the calculations, the lower energy peak at 287.1 eV originates from resonant transitions involving both CH and CH_2 1s carbon sites to their respective valence orbitals, with the contribution from the CH site being predominant (see Supplementary Materials). The higher energy peak at 287.6 eV corresponds, specifically, to transitions from CH_2 1s carbon sites to CH_2 valence orbitals. By tuning the photon energy to 287.1 eV or 287.6 eV, we can primarily excite the CH or the CH_2 carbon sites in adamantane, respectively.

After the core resonant excitation, the interplay between nuclear dynamics and electronic relaxation becomes crucial. We investigated the nuclear dynamics of adamantane following core resonant excitation using the equivalent core model [16,28]. The evolution of the molecular geometries in the core-excited states for the CH and CH_2 carbon sites are shown in Figure 1b,c, respectively. In the Z + 1 approximation, when a localized core–hole is created, the valence electrons in the molecule experience an effective nuclear charge that increases by one, which induces changes in bond distances, angles, and potential surfaces. We observe in Figure 1b that a localized CH core–hole state induced a change in the symmetry of adamantane from T_d to C_{3v}, which eventually led to the loss of one hydrogen atom. One the other hand, a localized CH_2 core–hole state induced a change in symmetry

of adamantane from T_d to C_{2v}, which elongated one C–H bond, which further changed to C_s symmetry and, eventually, led to loss of one hydrogen atome. Therefore, the localized core holes at the CH and CH_2 sites of adamantane exhibited distinct evolution patterns and significant distortion in the molecular geometry, which influence the subsequent Auger decay process and the fragmentation dynamics.

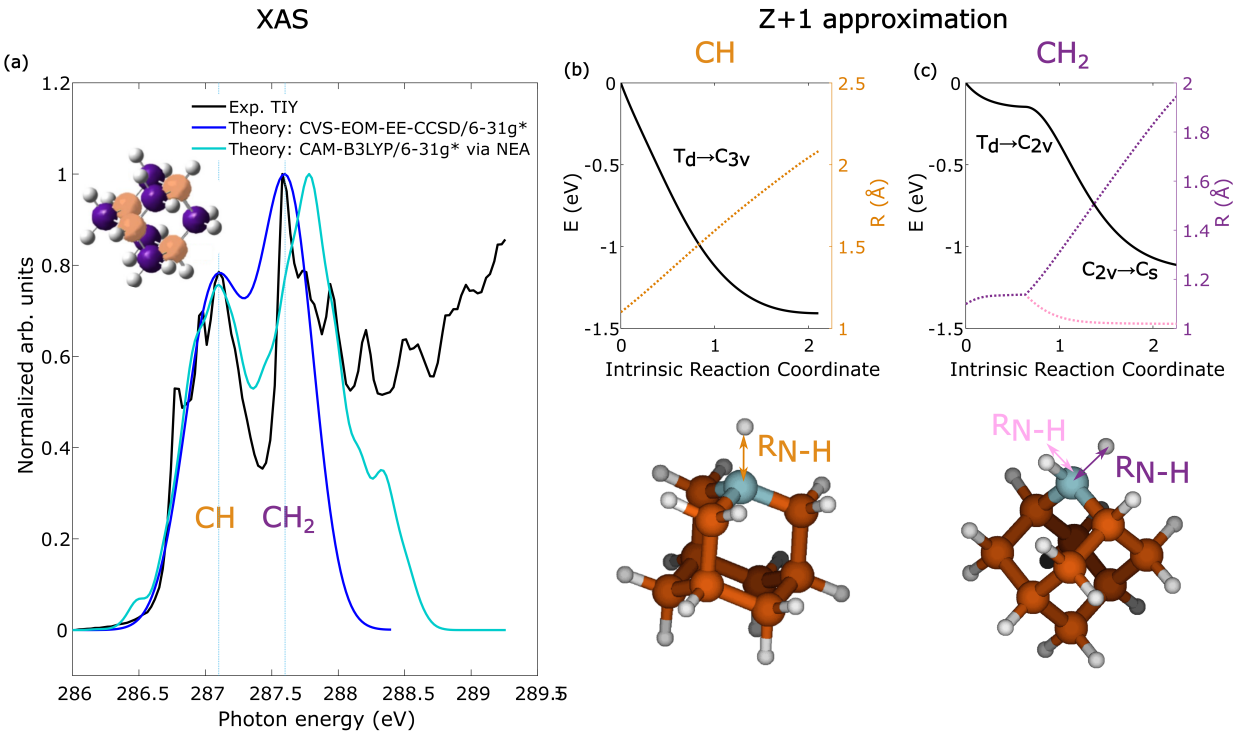

Figure 1. The experimental total ion yield (TIY) and the theoretical X-ray absorption (XAS) spectrum of adamantane below the C 1s ionization edge is shown in (**a**). The theoretical spectra were shifted to match the experiment, −3.60 eV for CVS-EOM-CCSD and 8.97 eV for CAM-B3LYP. The ground state carbon cage structure of the adamantane molecule with the highlighted CH (orange) and CH_2 (purple) sites is shown in the top left. The results from the equivalent core model [28] calculation with Z + 1 approximation for localized core holes at the CH and CH_2 carbon sites are shown in (**b**) and (**c**), respectively. The final calculated distorted geometry of the adamantane is shown below for the two carbon sites.

2.2. Resonant Auger Decay of Adamantane

Figure 2 shows the resonant Auger electron spectra (RAES) of adamantane for inner-shell resonant excitation to the CH (orange) and CH_2 (purple) valence orbitals lying at photon energies of 287.1 and 287.6 eV, respectively. The RAES is presented in the binding energy scale, calculated as the difference between the photon energy and the auger electron kinetic energy. In the RAES, the final states of the adamantane cation [29,30] (grey dashed lines) are assigned using the reference photo-emission spectrum of valence ionization (black) taken at an off-resonance photon energy of 285 eV. Two distinct regions were identified in the RAES, corresponding to participator Auger decay (1h) at the low binding energy (<17.5 eV), and spectatorAuger decay (2h-1p) at the high binding energy (>25 eV). By comparing to the off-resonant and the normal Auger spectra reported in our previous study [25], the region in the vicinity of the IT_2 is referred to as a *mixed* region, due to possible overlap of 1h and 2h–1p states [31–33]. The final Auger-populated states lying above the double ionization threshold (IT_2) at 23.9 eV auto-ionize to form adamantane dication. We observed that the CH site excitation was more likely to decay via participator, or mixed, Auger decay, whereas the CH_2 site excitation was more likely to decay via spectator Auger

decay. The strongest contribution in the RAES of the CH sites was observed at around 24.4 eV, and of the CH_2 sites at around 31.2 eV.

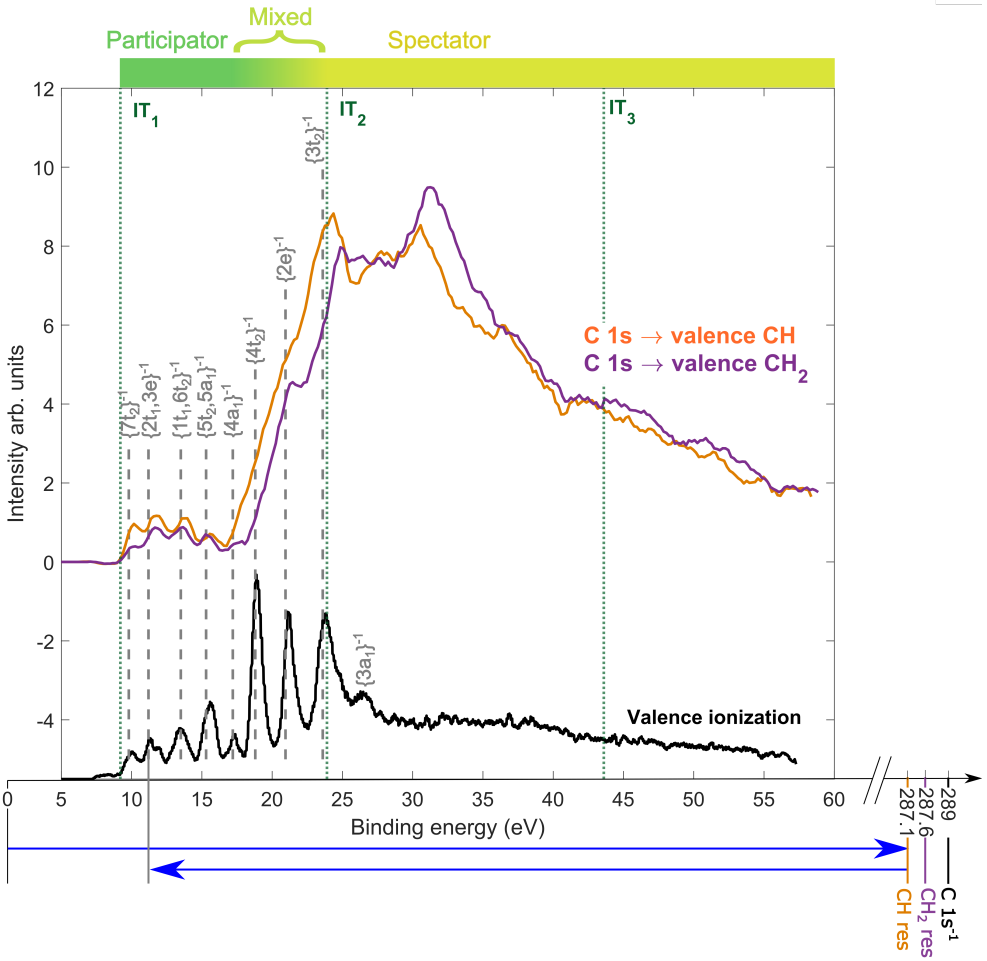

Figure 2. Resonant Auger electron spectra (top) of adamantane after CH and CH_2 resonant excitation at 287.1 eV and 287.6 eV, respectively, are shown in orange and purple, respectively. The off-resonance photoelectron spectrum (bottom) of valence ionization of adamantane at 285 eV is also shown in black. The assigned cation states [29,30] after participator Auger decay are shown in grey. Three distinct regions were identified in the spectrum, corresponding to participator, mixed and spectator Auger decay. The first, second and third ionization thresholds were labelled as (IT_1), (IT_2) and (IT_3), respectively. At the bottom, a simple energy level diagram shows the resonant excitations and Auger decays to final states (for instance the $\{2t_1/3e\}^{-1}$ cation state).

For binding energies below 25 eV, we calculated the theoretical participator Auger decay using the same level of theory as the XAS. The calculated participator Auger decay spectra at 287.1 eV and 287.6 eV are shown in Figure 3, with the experimental RAES. In the participator decay region below <17.5 eV, the theoretical RAES was in good agreement with the peak intensities of the 1h states in the experimental RAES at the two carbon sites. In the mixed decay region, however, the theoretical RAES only estimated the intensity of 1h states and was not able to replicate the mixed character of decay. We observed, in the experimental and theoretical RAES, that the probability of reaching states with t_2 symmetry was generally higher after CH excitation, suggesting a possible interplay between this electronic symmetry and the localization of the hole on the C–H bond. This hypothesis was corroborated by the difference between the spectra populating the cationic ground state, $7t_2^{-1}$, where the hole is reported to be localized on the C–H bond [34]. The theoretical RAES was calculated with frozen geometries and did not calculate the nuclear dynamics in the core-excited state. However, in the experimental RAES, the maximum

of many peaks shifted towards higher binding energy compared to the off-resonance spectrum. This reflected the nuclear wavepacket dynamics occurring in the core-excited states, such as those predicted by the Z + 1 approximation, which, after electronic relaxation. allow the reaching of potential energy surfaces outside the Franck–Condon region. Such nuclear dynamics lead, among other things, to vibrational excitation [35–37] and seem more pronounced after CH excitation than after CH_2 excitation. Therefore, we found a significant difference between the RAES of the CH and CH_2 sites. Our experimental and theoretical results showed that the "memory" of the localization of the initial core hole in adamantane was partly preserved after resonant Auger decay.

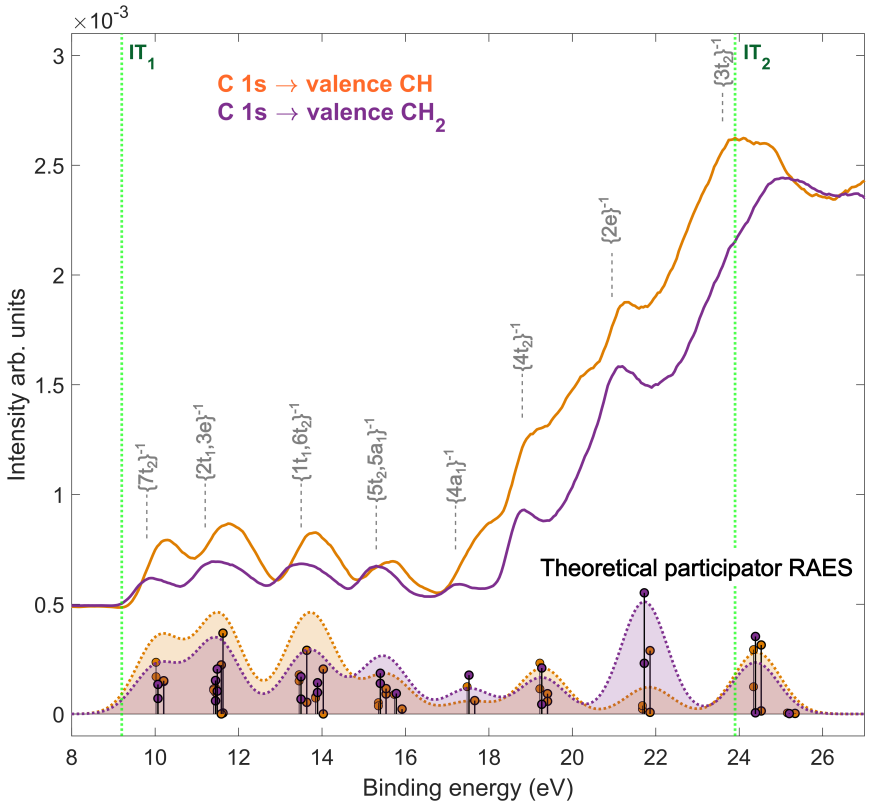

Figure 3. Experimental (top) and theoretical (bottom) resonant Auger electron spectra (RAES) of adamantane after CH and CH_2 resonant excitation at 287.1 eV and 287.6 eV, respectively, are shown in orange and purple, respectively. The theoretical spectra were shifted by 4.1 eV to match the experiment. The assigned cation states [29,30] after participator Auger decay are shown in grey. The first and second ionization thresholds were labeled as (IT_1) and (IT_2), respectively.

2.3. Site-Selective Fragmentation of Adamantane

We studied the fragmentation of adamantane ions after resonant Auger decay using Auger-electron photo-ion coincidence (AEPICO) spectroscopy. Our results, presented in Figure 4a,b, show that the fragment ions for both the CH and CH_2 sites were similar, consisting of a series of hydrocarbon fragments, $C_nH_x^+$, where x was mainly an odd number. The dominant ions for both sites were $C_3H_3^+$, $C_2H_3^+$, and $C_3H_5^+$, with the number of hydrogen atoms attached depending on the binding energy of the final Auger-populated state. This trend was clearly visible for the $C_4H_3^+$, $C_4H_5^+$ and $C_4H_7^+$ fragments in the AEPICO maps (Figure 4a,b). Our findings suggest that the final state energy influences hydrogen migration or evaporation during fragmentation. Additionally, for both sites, symmetric fragmentation of the carbon cage to form $C_5H_x^+$ fragments was unfavourable for all the final states. Figure 4c highlights the site-selectivity in fragmentation, showing the difference between the AEPICO plots for the CH and CH_2 sites. The areas in red had a higher yield for the CH site, while the areas in blue had a higher yield for the CH_2

site. Our data indicated that, after CH site excitation, the adamantane ions were more likely to dissociate into larger fragments, such as $C_6H_7^+$, $C_6H_9^+$, and $C_7H_9^+$, while the CH_2 site excitation resulted in dissociation into smaller fragments, such as $C_3H_3^+$ and $C_3H_5^+$. These differences in fragmentation appeared at different binding energies, suggesting that the site-selective Auger decay created statistical bias in the fragmentation pattern, with CH site excitation preferentially populating the adamantane cationic states and CH_2 site excitation resulting in Auger-populated dicationic states. In such a case, the fragmentation was actually state-specific, as previously reported for 2Br-pyrimidine [14]. The fragments $C_2H_3^+$, $C_3H_3^+$, $C_3H_5^+$, $C_6H_7^+$, and $C_7H_9^+$ had significant intensities in the difference AEPICO map (Figure 4c) and were, therefore, selected for further analysis of site-selectivity.

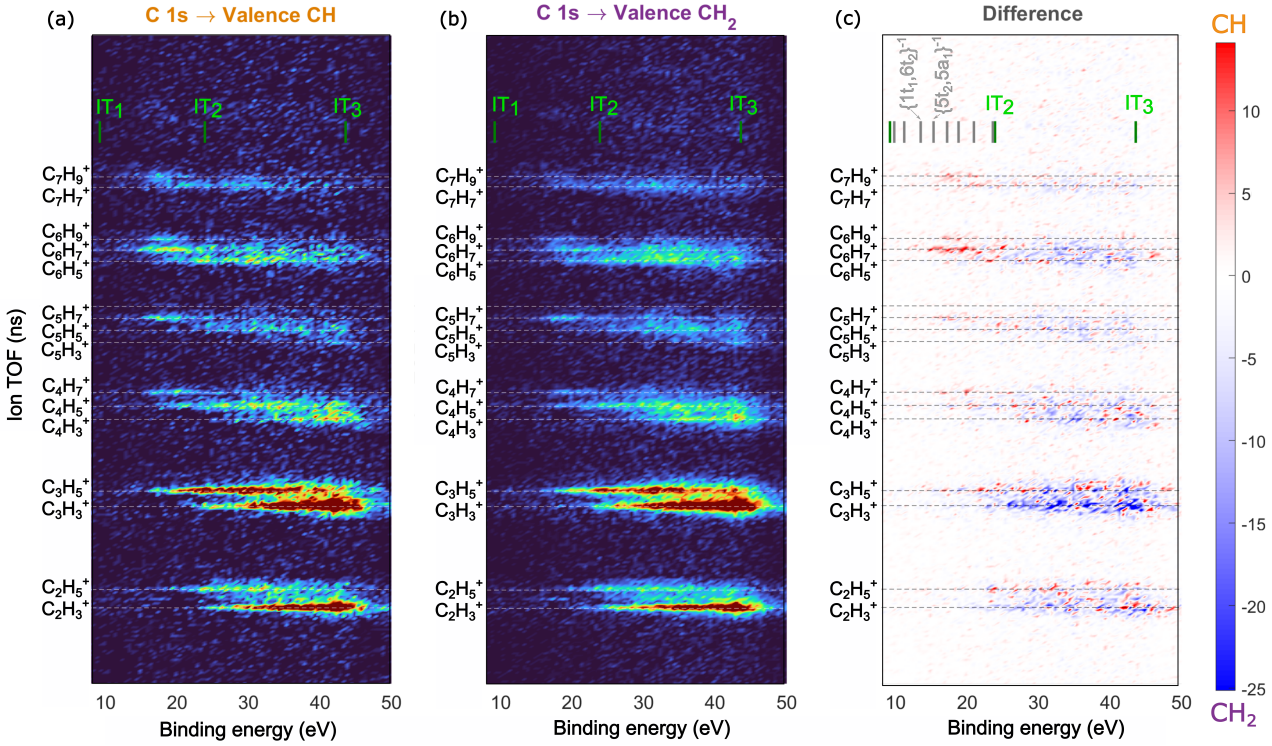

Figure 4. AEPICO map of ions and auger electrons detected in coincidence for the CH (**a**) and CH_2 (**b**) resonant excitations at 287.1 eV and 287.6 eV, respectively. The difference between the AEPICO maps (**a**,**b**) is shown in (**c**), the intensity in red indicates ions which had higher yield in (**a**) i.e., the CH site excitation and the intensity in blue indicates ions which had higher yield in (**b**) i.e., the CH_2 site excitation. The first, second and third ionization thresholds are labeled as (IT_1), (IT_2) and (IT_3), respectively. The maps (**a**,**b**) are area normalized.

In order to gain a deeper understanding of the fragmentation behavior of adamantane, we investigated whether final Auger-populated states with identical binding energies, resulting from excitation of the CH and CH_2 sites, exhibited discernible characteristics during fragmentation. The Auger electron energy-selected yield of ions in the AEPICO plot for the CH and CH_2 site excitations are presented in Figure 5a,b, respectively. These plots depict the relative yield of the selected ions as a function of the binding energy of the final Auger-populated states. The Auger-populated states located far below IT_2 represent the yield of cation fragmentation, while those close to, and above, IT_2 indicate the yield of dication fragmentation.

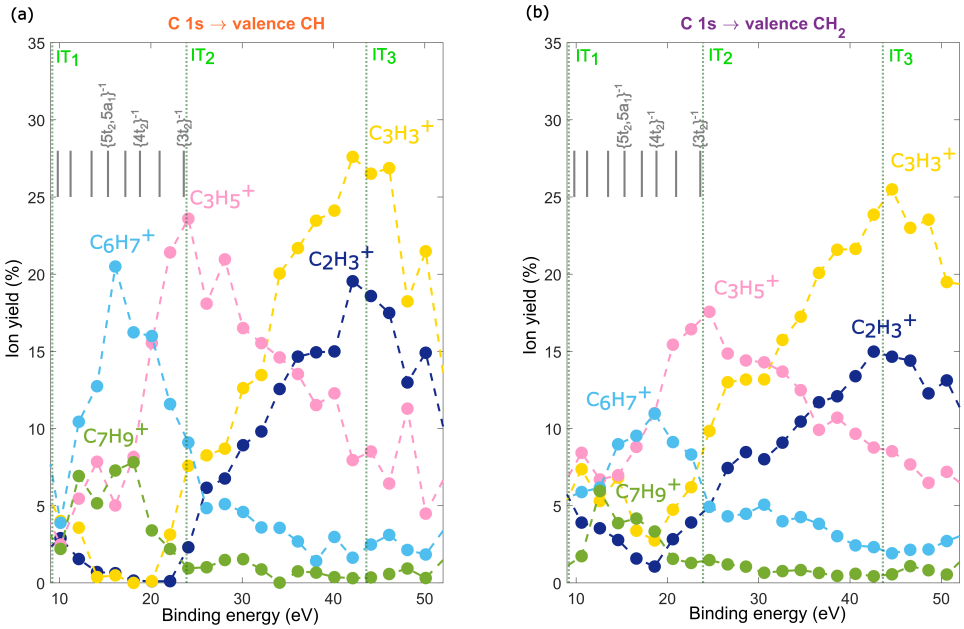

Figure 5. The energy-selected relative branching ratios of ions for the CH (**a**) and CH_2 (**b**) resonant excitations at 287.1 eV and 287.6 eV, respectively. The relative branching ratios were calculated from the AEPICO map by selecting the binding energy of the Auger-populated states. The assigned cation states after participator Auger decay are shown in grey. The first, second and third ionization thresholds are labeled as (IT_1), (IT_2) and (IT_3), respectively.

The fragmentation pattern of adamantane is influenced by the binding energy of the Auger-populated states, and the dominant fragment ion exhibits site-selectivity for states with binding energies lower than 30 eV. The dominant ion at lower binding energy states was $C_6H_7^+$, but it transitioned to $C_3H_5^+$ for states above 20 eV, and then to $C_3H_3^+$ for states above 30 eV, for both the CH and CH_2 sites. This transition in the yield of $C_6H_7^+$ and $C_3H_5^+$ was indicative of the onset of dication fragmentation [19] and suggested that the states above 20 eV underwent auto-ionization. The relative yields of $C_6H_7^+$ and $C_3H_5^+$ were site-selective and state-specific. In the case of CH site excitation, we observed that cationic states preferentially fragmented into $C_6H_7^+$, with a neutral fragment C_4H_9. The yield of this fragmentation channel was highest (20.5%) at a binding energy of about 16 eV and could be correlated to the nearly degenerate $5t_2$,$5a_1{}^{-1}$ states. In contrast, in the case of CH_2 site excitation, the relative yield showed that cation fragmentation could lead to either $C_6H_7^+$ or $C_3H_5^+$ fragments. The yield of $C_6H_7^+$ was only slightly enhanced, with a maximum (11%) at 18.5 eV, which could be correlated to the $4t_2{}^{-1}$ state. Additionally, the yield of $C_7H_9^+$ was also site-selective. For the CH site, the yield was highest (~8%) in the range of 12 to 18 eV, but for the CH_2 site, the yield was highest at 12.6 eV and decreased drastically at higher binding energies. These results suggested that cationic states reached after participator Auger decay displayed site-selectivity, and that the memory of the core–hole location influenced cationic fragmentation to some extent. In contrast, for spectator Auger-populated states, the initial core–hole location did not affect the fragmentation pathway, and the dications produced mainly $C_3H_3^+$ and $C_2H_3^+$ ions for both sites. The difference in the yield of $C_3H_3^+$ was a result of site-dependent Auger decay, which led to a higher probability of reaching favourable final states after CH_2 site excitation. However, when the relative yield of ions at these higher binding energy states was examined, the yield of $C_3H_3^+$ was the same for both sites.

The difference in the yield of $C_6H_7^+$ and $C_7H_9^+$ was attributed to the distinct properties of the final Auger-populated states with the same binding energy, which dissociated differently for the two sites, with a preference for the CH site. The maximum yield

of these fragments could be correlated to the nearly degenerated $5t_2/5a_1$ states, while their yields vanished after the $4t_2$ states. In comparison, these fragmentation channels were less favourable after CH_2 excitation. The presence of states with t_2 symmetry was in line with our electron spectroscopy observations and supported the idea that some states with this electronic symmetry reflect the localization of a hole on a C–H bond. The localization of a hole on the C–H bond leads to distortion of the adamantane cation [34], involving elongation of three C–C bonds and the formation of C_6H_9 and C_4H_7 units, in concurrence with the observation of the $C_6H_7^+$ fragment. However, other factors, such as an increase in the internal rovibrational energy, must be taken into consideration to account for the disappearance of these fragments. Such factors can cause the emission of neutral hydrogen atoms or the cleavage of C–C bonds. It should be noted that these fragments have been shown to reveal information on the cage-opening mechanisms at lower excitation energies [18], suggesting that the cage-opening mechanism of the adamantane cation is site-sensitive.

2.4. Comparision to Core-Ionized Adamantane

The mass spectrum of ions produced from the fragmentation of adamantane dication following core excitation of the CH and CH_2 sites and core ionization is shown in Figure 6. The mass spectrum was calculated as projections of Auger-electron Photoion–Photoion coincidence (AE-PIPICO) maps. In our previous AE-PIPICO study [25], we speculated that site-sensitive fragmentation of adamantane dication after core-ionization indirectly used theoretical normal Auger decay calculations. Here, we directly studied site-selective fragmentation using core excitation. We observed that, for both the CH and CH_2 sites, the mass spectrum was rather similar, with dominant ions $C_3H_3^+$, $C_2H_3^+$ and $C_3H_5^+$. Therefore, the fragmentation of the adamantane dication did not exhibit site selectivity and likely depended only on the internal energy of the dicationic state. However, the fragmentation of dication is different following core excitation and core ionization. In the core ionization case, the dominant ions are $C_2H_3^+$, $C_3H_3^+$, $C_3H_5^+$ and CH_3^+ with broad peaks, due to higher kinetic energy release compared to the core excitation case.

Maclot et al. [20] showed that the fragmentation of adamantane dication involves barrier-free structural changes, such as hydrogen migration(s) or cage-opening, before dissociating into different ion pairs $C_nH_x^+/C_mH_y^+$. The hydrogen migrations result in the open-cage geometry of adamantane, with CH_3 termination(s). The lowest energy open-cage structure of adamantane dication is shown in blue. In comparison to core-ionization, the cage opening mechanism seems fundamentally different for core excitation of the CH and CH_2 sites, since the intensity of the methylium (CH_3^+) ion (peak highlighted with a red arrow) decreases by 44% in the AE-PIPICO mass spectrum. Within the Z + 1 approximation, we found that the symmetry broke after CH and CH_2 excitation and could lead to hydrogen loss in the core–hole state. During the lifetime of the core–hole, ultrafast nuclear dynamics, mainly of hydrogen atoms, contribute to a distortion of the adamantane cage. In such cases, the calculations reported by Maclot et al. [20] would not be valid for our core excitation studies. One could speculate that rather large transient species are produced; for instance, containing 4 and 6 carbons, instead of the intact open-cage geometry. Nevertheless, there is a difference in the fragmentation of the adamantane dication after core excitation compared to core ionization. This difference may be attributed to the distinct ultrafast dynamics that occur in the core–hole and dication states leading to the fragmentation.

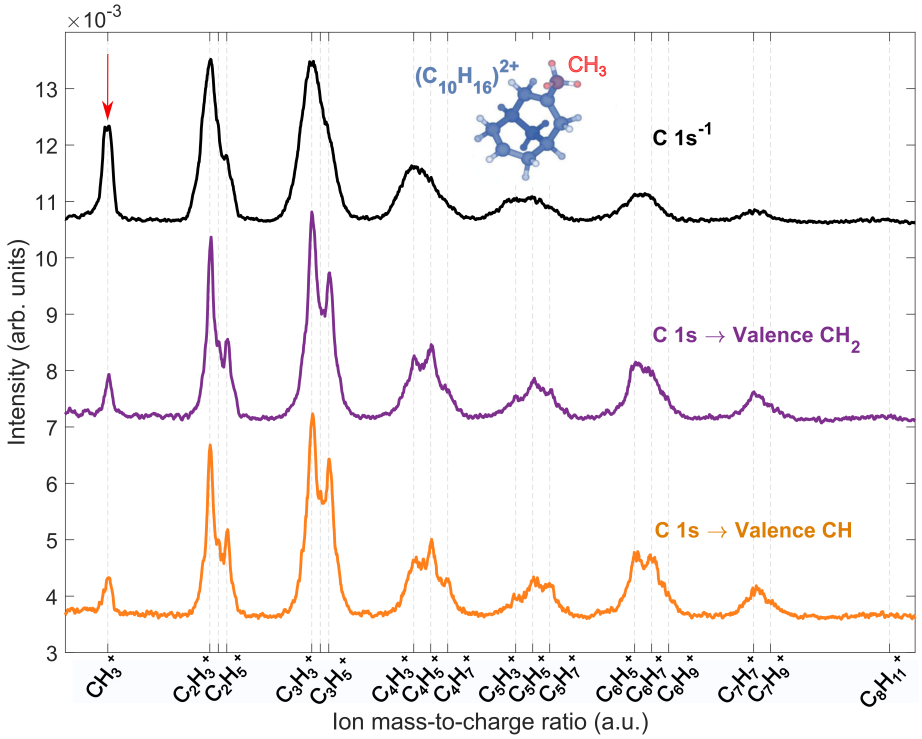

Figure 6. The mass spectrum of adamantane dication fragmentation after CH (orange) and CH_2 (purple) resonant excitations at 287.1 eV and 287.6 eV, respectively, and core ionization (black) at 350 eV. The mass spectrum was added up from projections of the 2D AE-PIPICO map. The lowest energy open-cage geometry [20] of adamantane dication with one CH_3 termination is shown in blue. The difference in the intensity of the methylium (CH_3^+) peak is highlighted with a red arrow.

3. Methods

3.1. Experimental

The experiments were conducted at PLEIADES soft X-ray beamline at Synchrotron SOLEIL [38]. The Apple II HU 80 permanent magnet undulator generated the soft X-rays, which were monochromatized using the modified Petersen plane grating monochromator, with a high-flux 600 lines per mm grating. The CO_2 C-1s $\rightarrow \pi^*$ absorption peak [39] was used to calibrate the photon energy for the present experiment. A heated gas cell [25] was used, with a VG-Scienta R4000 electron energy analyzer, to perform electron spectroscopy measurements [40]. The high-purity commercial adamantane powder (99%, Sigma-Aldrich, Saint-Quentin-Fallavier, France) was used as a sample without further purification. During the measurements, the gas cell was heated at 54 degrees Celsius, and the pressure in the Scienta chamber was 7.1×10^{-7} mbar. The X-ray absorption spectrum was taken with the total ion yield technique and a resolution of 25 meV. The kinetic energy scale of the adamantane Auger spectra was calibrated according to the measured CO_2 Auger spectrum and the position of reference lines reported by Modeman et al. [41]. The Auger electron spectra of adamantane were recorded at a photon energy of 287.1 and 287.6 eV with an overall resolution of 55 meV.

The EPICEA setup [15,42], consisting of a double toroidal electron analyzer (DTA) [43] and a 3D focusing ion TOF spectrometer, was used to record the Auger-electron photo-ion coincidence (AEPICO) and Auger-electron photoion–photoion coincidence (AE-PIPICO) data. Electrons emitted at an angle of 54.7° were retarded to a predetermined pass energy (Ep) in the DTA. The detection electron kinetic energy window was about 12% of the defined Ep, whereas the energy resolution was about 1% of the Ep. In the present experiments, a pass energy of 250 eV was used, which led to an analyzer resolution of about 2.5 eV and a detection range of ±15 eV. The calibration of the kinetic energy scale was

performed using Xe 5p and Xe 5s IPs as reference lines. The kinetic energy scale calibration was achieved by using a previously proposed empirical formula [44] to transform the detector radius position (mm) to the electron kinetic energy (eV). The adamantane was introduced into the vacuum chamber through a heated injection gas line and a heated needle in a crossed-beam experimental arrangement. In the EPICEA setup, the detection of an electron triggers a pulsed field that accelerates all ions toward a 3D momentum mass spectrometer. Hence, a coincidence event consists of an energy analyzed electron, positions on the detector and time of flight of all extracted ions. Additionally, a pulse generator was used to produce random triggers, which extracted ions present in the interaction. This allowed us to subtract the background ion signal, the *false* coincidences, using the procedure reported by Prumper et al. [45].

3.2. Theoretical

The X-ray absorption spectra (XAS) were modeled at the CVS-EOM-CCSD level with 6-31g* and 6-31+g* basis sets for the structure optimized in the ground state at the CAM-B3LYP/6-31+g* level. Furthermore, the spectra were modeled at various TDDFT levels, via the nuclear ensemble approach (NEA). The character of the excitations was studied via natural transition orbitals. The RAES were modeled in terms of the Feschbach–Fano theory [46,47] at the EOM-CCSD level with 6-31g* and 6-31+g* basis sets, as implemented in Q-Chem [48]. All details are provided in the Supplementary Materials.

We also performed simulations in the frame of the Z + 1 approximation. To do this, we considered the initial geometry that optimized the neutral adamantane in the ground state was at the B3LYP/6-31g* level. Then, substituting one C atom with one N atom, and keeping a neutral charge, we explored the potential energy surface, allowing the geometry to relax, following the minimum energy path (downhill) up to a minimum being reached, using the same level of theory—B3LYP/6-31g*. These calculations were performed with the Gaussian16 program [49].

4. Conclusions

We studied the fragmentation dynamics of adamantane after resonant inner-shell excitation using a state-of-the-art coincidence technique between Auger electrons and ions in combination with advanced theoretical calculations. The resonant Auger decay spectra provided evidence, and, in particular, the electronic states with a t_2 symmetry, of there being memory of the localization of the initial core–hole upon resonant excitation to the CH or CH_2 valence orbitals. After *participator* Auger decay, the fragmentation of the molecules leading to large fragments with 6–7 carbon atoms exhibited a clear site-sensitivity of the initial core–hole localization, proving that different carbon sites could lead to different cage opening mechanisms. After *spectator* Auger decay in the double ionization continua, the fragmentation dynamics was drastically different to that observed after core–hole ionization. The absence of the methyl group, in coincidence with a large fragment, suggested that the cage opening mechanisms led to rather large short-lived species, which eventually underwent further fragmentation.

Supplementary Materials: The following supporting information can be downloaded at: https://www.mdpi.com/article/10.3390/molecules28145510/s1, Figure S1: XAS spectra of adamantane. Panel A shows spectra calculated at the TDDFT/CAMB3LYP, BMK and at CVS-EOM-EE-CCSD levels with various basis sets for the minimum energy structure. The spectra were phenomenologically broadened by 0.2 eV. Panel B shows the spectra within the NEA at various levels of theory calculated for 200 structures from MD. Each point was phenomenologically broadened by 0.05 eV. Spectra were shifted to match the position of the first experimental peak located at 287.1 eV as such: panel (a): CAM-B3LYP/6-31g* → +8.87 eV — CAM-B3LYP/6-31+g* → +10.50 eV — CAM-B3LYP/6-31++g** → +10.67 eV — BMK/6-311++g** → +4.40 eV — CVS-EOM-CCSD/6-31g* → −3.58 eV — CVS-EOM-CCSD/6-31+g* → −1.75 eV and panel (b): CAM-B3LYP/6-31g* → +8.97 eV — CAM-B3LYP/6-31+g* → +10.51 eV — CAM-B3LYP/6-31++g** → +10.98 eV — CAM-B3LYP/cc-pCVTZ → +10.29 eV — BMK/6- 311++g** → +4.30 eV; Figure S2: Natural transition orbitals (NTO) calculated at the CVS-

EOM-EE-CCSD/6-31g* level for the lowest energy transitions. The lower energy peak in the XAS spectrum corresponds to a combination of excitations from the 1s carbon sites to CH and CH2 valence orbitals. Excitations are labeled as A and B. The higher energy peak corresponds to the C 1s → valence CH2 orbital excitation, labeled as excitation C; Figure S3: The valence band XPS spectra for the minimum energy structure calculated at the EOMIP- CCSD level using various basis sets. Each ionization energy was phenomenological Gaussian broadened by 0.2 eV. The intensities were estimated as the norms of the respective Dyson orbitals; Figure S4: The resonant Auger spectra for the minimum energy structure calculated within the EOM-CCSD framework level using 6-31g* (upper panel) and 6-31+g* (lower panel) basis sets. Each energy was phenomenological Gaussian broadened by 0.2 eV. The spectra in the upper panel were shifted by 4.15 eV and in the lower panel by 2.5 eV to higher energies to match the experimental spectra. References [46–48,50–69] are cited in the supplementary materials.

Author Contributions: A.R.M., P.R. and S.M. performed the experiments; S.G. and S.M. analyzed the data; E.M. calculated the theoretical XAS and RAES; S.D.-T. calculated the Z + 1 approximation and the adamantane dication structure. All authors participated to the scientific discussions concerning the interpretation of the results. S.G. and M.G. wrote this manuscript and all authors helped to improve it. All authors have read and agreed to the published version of the manuscript

Funding: The research leading to this result has been supported by the project CALIPSOplus under Grant Agreement 730872 from the EU Framework Programme for Research and Innovation HORIZON 2020 and the COST Action CA18212—Molecular Dynamics in the GAS phase (MD-GAS), supported by COST (European Cooperation in Science and Technology). We also acknowledge the support of the Helmholtz Foundation through the Helmholtz-Lund International Graduate School (HELIOS, HIRS-0018) and the Swedish Research Council (VR2020-0520). R.F. thanks the Swedish Research Council and the Knut and Alice Wallenberg Foundation for financial support. This work was partially supported by MICINN (Spanish Ministry of Science and Innovation) project PID2019-110091GB-I00 funded by MCIN/AEI/10.13039/501100011033, and the "María de Maeztu" (CEX2018-000805-M) Program for Centers of Excellence in RD and Czech Science Foundation, project no. 21-26601X (EXPRO).

Institutional Review Board Statement: Not applicable.

Informed Consent Statement: Not applicable.

Data Availability Statement: The data presented in this study are available on request from the corresponding author.

Acknowledgments: This work was performed on the PLEIADES beamline of synchrotron SOLEIL under the proposal no. 20191168. We acknowledge SOLEIL for access to the synchrotron radiation facilities and we would like to thank the PLEAIDES beamline team for their assistance. The authors acknowledge the generous allocation of computer time at the Centro de Computación Científica at the Universidad Autónoma de Madrid (CCC-UAM).

Conflicts of Interest: The authors declare no conflict of interest.

Sample Availability: Not available.

References

1. Eberhardt, W.; Sham, T.; Carr, R.; Krummacher, S.; Strongin, M.; Weng, S.; Wesner, D. Site-specific fragmentation of small molecules following soft-X-ray excitation. *Phys. Rev. Lett.* **1983**, *50*, 1038. [CrossRef]
2. Nenner, I.; Reynaud, C.; Schmelz, H.; Ferrand-Tanaka, L.; Simon, M.; Morin, P. Site selective fragmentation with soft X-rays: From gaseous polyatomic molecules, free clusters, polymers, adsorbates to biological macromolecules. *Z. Phys. Chem.* **1996**, *195*, 43–63. [CrossRef]
3. Hatherly, P.; Codling, K.; Stankiewicz, M.; Roper, M. Symmetry effects in site-specific fragmentation of carbon dioxide. *J. Electron Spectrosc. Relat. Phenom.* **1996**, *79*, 407–410. [CrossRef]
4. Hitchcock, A.P.; Neville, J.J.; Ju, A.; Cavell, R.G. Ionic fragmentation of inner-shell excited molecules. *J. Electron Spectrosc. Relat. Phenom.* **1998**, *88*, 71–75. [CrossRef]
5. Ibuki, T.; Okada, K.; Saito, K.; Gejo, T. Molecular size effect on the site-specific fragmentation of N and OK shell excited CH_3OCOCN and CH_3OCOCH_2CN molecules. *J. Electron Spectrosc. Relat. Phenom.* **2000**, *107*, 39–47. [CrossRef]

6. Liu, X.; Prümper, G.; Kukk, E.; Sankari, R.; Hoshino, M.; Makochekanwa, C.; Kitajima, M.; Tanaka, H.; Yoshida, H.; Tamenori, Y.; et al. Site-selective ion production of the core-excited CH_3 F molecule probed by auger-electron–ion coincidence measurements. *Phys. Rev. A* **2005**, *72*, 042704. [CrossRef]
7. Erben, M.F.; Geronés, M.; Romano, R.M.; Della Védova, C.O. Dissociative photoionization of methoxycarbonylsulfenyl chloride, $CH_3OC(O)SCl$, following sulfur 2p, chlorine 2p, and oxygen 1s excitations. *J. Phys. Chem. A* **2007**, *111*, 8062–8071. [CrossRef]
8. Salén, P.; Kamińska, M.; Squibb, R.J.; Richter, R.; Alagia, M.; Stranges, S.; van der Meulen, P.; Eland, J.H.; Feifel, R.; Zhaunerchyk, V. Selectivity in fragmentation of N-methylacetamide after resonant K-shell excitation. *Phys. Chem. Chem. Phys.* **2014**, *16*, 15231–15240. [CrossRef]
9. de Castilho, R.; Nunez, C.; Lago, A.F.; Santos, A.C.F.; Coutinho, L.H.; Lucas, C.A.; Pilling, S.; Silva-Moraes, M.; de Souza, G. Excitation and ionic fragmentation of the carvone molecule ($C_{10}H_{14}O$) around the O 1s edge. *J. Electron Spectrosc. Relat. Phenom.* **2014**, *192*, 61–68. [CrossRef]
10. Chagas, G.R.; Satyanarayana, V.S.V.; Kessler, F.; Belmonte, G.K.; Gonsalves, K.E.; Weibel, D.E. Selective fragmentation of radiation-sensitive novel polymeric resist materials by inner-shell irradiation. *ACS Appl. Mater. Interfaces* **2015**, *7*, 16348–16356. [CrossRef]
11. Habenicht, W.; Baiter, H.; Mueller-Dethlefs, K.; Schlag, E.W. Memory effects in molecular fragmentation induced by site-specific core excitation using a reflection time-of-flight mass spectrometer. *J. Phys. Chem.* **1991**, *95*, 6774–6780. [CrossRef]
12. Nagaoka, S.i.; Fujibuchi, T.; Ohshita, J.; Ishikawa, M.; Koyano, I. Fragmentation of $F_3SiCH_2CH_2Si(CH_3)_3$ vapour following Si: 2p core-level photoexcitation. A search for a site-specific process in complex molecules. *Int. J. Mass Spectrom. Ion Process.* **1997**, *171*, 95–103. [CrossRef]
13. Schmelz, H.; Reynaud, C.; Simon, M.; Nenner, I. Site-selective fragmentation in core-excited bromo-chloro-alkanes [$Br(CH_2)nCl$]. *J. Chem. Phys.* **1994**, *101*, 3742–3749. [CrossRef]
14. Bolognesi, P.; Kettunen, J.; Cartoni, A.; Richter, R.; Tosic, S.; Maclot, S.; Rousseau, P.; Delaunay, R.; Avaldi, L. Site-and state-selected photofragmentation of 2Br-pyrimidine. *Phys. Chem. Chem. Phys.* **2015**, *17*, 24063–24069. [CrossRef] [PubMed]
15. Gerlach, M.; Fantuzzi, F.; Wohlfart, L.; Kopp, K.; Engels, B.; Bozek, J.; Nicolas, C.; Mayer, D.; Gühr, M.; Holzmeier, F.; et al. Fragmentation of isocyanic acid, HNCO, following core excitation and ionization. *J. Chem. Phys.* **2021**, *154*, 114302. [CrossRef] [PubMed]
16. Oghbaiee, S.; Gisselbrecht, M.; Walsh, N.; Oostenrijk, B.; Laksman, J.; Månsson, E.P.; Sankari, A.; Eland, J.H.; Sorensen, S.L. Site-dependent nuclear dynamics in core-excited butadiene. *Phys. Chem. Chem. Physics* **2022**, *24*, 28825–28830. [CrossRef]
17. Levola, H.; Itälä, E.; Schlesier, K.; Kooser, K.; Laine, S.; Laksman, J.; Ha, D.T.; Rachlew, E.; Tarkanovskaja, M.; Tanzer, K.; et al. Ionization-site effects on the photofragmentation of chloro-and bromoacetic acid molecules. *Phys. Rev. A* **2015**, *92*, 063409. [CrossRef]
18. Candian, A.; Bouwman, J.; Hemberger, P.; Bodi, A.; Tielens, A.G. Dissociative ionisation of adamantane: A combined theoretical and experimental study. *Phys. Chem. Chem. Phys.* **2018**, *20*, 5399–5406. [CrossRef]
19. Boyer, A.; Hervé, M.; Scognamiglio, A.; Loriot, V.; Lépine, F. Time-resolved relaxation and cage opening in diamondoids following XUV ultrafast ionization. *Phys. Chem. Chem. Phys.* **2021**, *23*, 27477–27483. [CrossRef]
20. Maclot, S.; Lahl, J.; Peschel, J.; Wikmark, H.; Rudawski, P.; Brunner, F.; Coudert-Alteirac, H.; Indrajith, S.; Huber, B.A.; Díaz-Tendero, S.; et al. Dissociation dynamics of the diamondoid adamantane upon photoionization by XUV femtosecond pulses. *Sci. Rep.* **2020**, *10*, 2884. [CrossRef]
21. Bouwman, J.; Horst, S.; Oomens, J. Spectroscopic characterization of the product ions formed by electron ionization of adamantane. *ChemPhysChem* **2018**, *19*, 3211–3218. [CrossRef] [PubMed]
22. Waltman, R.J.; Ling, A.C. Mass spectrometry of diamantane and some adamantane derivatives. *Can. J. Chem.* **1980**, *58*, 2189–2195. [CrossRef]
23. Crandall, P.B.; Müller, D.; Leroux, J.; Förstel, M.; Dopfer, O. Optical spectrum of the adamantane radical cation. *Astrophys. J. Lett.* **2020**, *900*, L20. [CrossRef]
24. Richter, R.; Wolter, D.; Zimmermann, T.; Landt, L.; Knecht, A.; Heidrich, C.; Merli, A.; Dopfer, O.; Reiß, P.; Ehresmann, A.; et al. Size and shape dependent photoluminescence and excited state decay rates of diamondoids. *Phys. Chem. Chem. Phys.* **2014**, *16*, 3070–3076. [CrossRef]
25. Ganguly, S.; Gisselbrecht, M.; Eng-Johnsson, P.; Feifel, R.; Hervieux, P.A.; Alfaytarouni, Z.; Fink, R.F.; Díaz-Tendero, S.; Milosavljević, A.R.; Rousseau, P.; et al. Coincidence study of core-ionized adamantane: Site-sensitivity within a carbon cage? *Phys. Chem. Chem. Phys.* **2022**, *24*, 28994–29003. [CrossRef]
26. Willey, T.; Bostedt, C.; Van Buuren, T.; Dahl, J.; Liu, S.; Carlson, R.; Terminello, L.; Möller, T. Molecular limits to the quantum confinement model in diamond clusters. *Phys. Rev. Lett.* **2005**, *95*, 113401. [CrossRef]
27. Willey, T.M.; Lee, J.R.; Brehmer, D.; Paredes Mellone, O.A.; Landt, L.; Schreiner, P.R.; Fokin, A.A.; Tkachenko, B.A.; de Meijere, A.; Kozhushkov, S.; et al. X-ray spectroscopic identification of strain and structure-based resonances in a series of saturated carbon-cage molecules: Adamantane, twistane, octahedrane, and cubane. *J. Vac. Sci. Technol. A Vacuum Surf. Film.* **2021**, *39*, 053208. [CrossRef]
28. Kryzhevoi, N.V.; Dobrodey, N.V.; Cederbaum, L.S. Equivalent core model: Extended theory and applications. *J. Chem. Phys.* **2003**, *118*, 2081–2091. [CrossRef]

29. Morini, F.; Watanabe, N.; Kojima, M.; Deleuze, M.S.; Takahashi, M. Influence of molecular vibrations on the valence electron momentum distributions of adamantane. *J. Chem. Phys.* **2017**, *146*, 094307. [CrossRef]
30. Boschi, R.; Schmidt, W.; Suffolk, R.; Wilkins, B.; Lempka, H.; Ridyard, J. Complete valence shell electronic structure of adamantane from He I and He II photoelectron spectroscopy. *J. Electron Spectrosc. Relat. Phenom.* **1973**, *2*, 377–380. [CrossRef]
31. Sałek, P.; Fink, R.; Gel'mukhanov, F.; Piancastelli, M.; Feifer, R.; Bässler, M.; Sorensen, S.; Miron, C.; Wang, H.; Hjelte, I.; et al. Resonant X-ray Raman Scattering involving avoided crossings in the final-state potential-energy curves. *Phys. Rev. A* **2000**, *62*, 062506. [CrossRef]
32. Piancastelli, M.; Fink, R.; Feifel, R.; Bässler, M.; Sorensen, S.; Miron, C.; Wang, H.; Hjelte, I.; Björneholm, O.; Ausmees, A.; et al. Bond-distance-dependent decay probability of the N 1s→ π^* core-excited state in N_2. *J. Phys. B At. Mol. Opt. Phys.* **2000**, *33*, 1819. [CrossRef]
33. Feifel, R.; Piancastelli, M.N. Core-level spectroscopy and dynamics of free molecules. *J. Electron Spectrosc. Relat. Phenom.* **2011**, *183*, 10–28. [CrossRef]
34. Patzer, A.; Schütz, M.; Möller, T.; Dopfer, O. Infrared spectrum and structure of the adamantane cation: Direct evidence for Jahn–Teller distortion. *Angew. Chem.* **2012**, *124*, 5009–5013. [CrossRef]
35. Miron, C.; Simon, M.; Morin, P.; Nanbu, S.; Kosugi, N.; Sorensen, S.; Naves de Brito, A.; Piancastelli, M.; Björneholm, O.; Feifel, R.; et al. Nuclear motion driven by the Renner–Teller effect as observed in the resonant Auger decay to the X2Π electronic ground state of N_2O+. *J. Chem. Phys.* **2001**, *115*, 864–869. [CrossRef]
36. Antonsson, E.; Patanen, M.; Nicolas, C.; Benkoula, S.; Neville, J.; Sukhorukov, V.; Bozek, J.; Demekhin, P.V.; Miron, C. Dynamics of the C 1 s→ π^* excitation and decay in CO_2 probed by vibrationally and angularly resolved Auger spectroscopy. *Phys. Rev. A* **2015**, *92*, 042506. [CrossRef]
37. Travnikova, O.; Miron, C.; Bässler, M.; Feifel, R.; Piancastelli, M.; Sorensen, S.; Svensson, S. Resonant Auger decay study of C1s→ π^* core-excited OCS. *J. Electron Spectrosc. Relat. Phenom.* **2009**, *174*, 100–106. [CrossRef]
38. PLEIADES Beamline Website. 2019. Available online: https://www.synchrotron-soleil.fr/fr/lignes-de-lumiere/pleiades (accessed on 1 June 2021).
39. Adachi, J.i.; Kosugi, N.; Shigemasa, E.; Yagishita, A. Vibronic Couplings in the C 1s→ n sσg Rydberg Excited States of CO_2. *J. Phys. Chem.* **1996**, *100*, 19783–19788. [CrossRef]
40. Danilovic, D.; Bozanic, D.K.; Dojcilovic, R.; Vukmirovic, N.; Sapkota, P.; Vukasinovic, I.; Djokovic, V.; Bozek, J.; Nicolas, C.; Ptasinska, S.; et al. Aerosol Synthesis and Gas-Phase Photoelectron Spectroscopy of Ag-Bi-I Nanosystems. *J. Phys. Chem. C* **2020**, *124*, 23930–23937. [CrossRef]
41. Moddeman, W.; Carlson, T.A.; Krause, M.O.; Pullen, B.; Bull, W.; Schweitzer, G. Determination of the K—LL auger spectra of N_2, O_2, CO, NO, H_2O, and CO_2. *J. Chem. Phys.* **1971**, *55*, 2317–2336. [CrossRef]
42. Liu, X.J.; Nicolas, C.; Robert, E.; Miron, C. EPICEA: Probing high-energy electron emission in the molecular frame. *J. Phys. Conf. Ser.* **2014**, *488*, 142005. [CrossRef]
43. Miron, C.; Simon, M.; Leclercq, N.; Morin, P. New high luminosity "double toroidal" electron spectrometer. *Rev. Sci. Instruments* **1997**, *68*, 3728–3737. [CrossRef]
44. Liu, X.J.; Nicolas, C.; Miron, C. Design of a lens table for a double toroidal electron spectrometer. *Rev. Sci. Instruments* **2013**, *84*, 033105. [CrossRef] [PubMed]
45. Prümper, G.; Ueda, K. Electron–ion–ion coincidence experiments for photofragmentation of polyatomic molecules using pulsed electric fields: Treatment of random coincidences. *Nucl. Instruments Methods Phys. Res. Sect. A Accel. Spectrometers Detect. Assoc. Equip.* **2007**, *574*, 350–362. [CrossRef]
46. Skomorowski, W.; Krylov, A.I. Feshbach-Fano approach for calculation of Auger decay rates using equation-of-motion coupled-cluster wave functions. I. Theory and implementation. *J. Chem. Phys.* **2021**, *154*, 084124. [CrossRef]
47. Skomorowski, W.; Krylov, A.I. Feshbach–Fano approach for calculation of Auger decay rates using equation-of-motion coupled-cluster wave functions. II. Numerical examples and benchmarks. *J. Chem. Phys.* **2021**, *154*, 084125. [CrossRef]
48. Epifanovsky, E.; Gilbert, A.T.; Feng, X.; Lee, J.; Mao, Y.; Mardirossian, N.; Pokhilko, P.; White, A.F.; Coons, M.P.; Dempwolff, A.L.; et al. Software for the frontiers of quantum chemistry: An overview of developments in the Q-Chem 5 package. *J. Chem. Phys.* **2021**, *155*, 084801. [CrossRef]
49. Frisch, M.J.; Trucks, G.W.; Schlegel, H.B.; Scuseria, G.E.; Robb, M.A.; Cheeseman, J.R.; Scalmani, G.; Barone, V.; Petersson, G.A.; Nakatsuji, H.; et al. *Gaussian~16 Revision C.01*; Gaussian Inc.: Wallingford, CT, USA, 2016.
50. Frisch, M.; Trucks, G.; Schlegel, H.; Scuseria, G.; Robb, M.; Cheeseman, J.; Scalmani, G.; Barone, V.; Petersson, G.; Nakatsuji, H.; et al. *Gaussian 09, revision a.02*; Gaussian Inc.: Wallingford, CT, USA, 2016.
51. Ceriotti, M.; Bussi, G.; Parrinello, M. Nuclear quantum effects in solids using a colorednoise thermostat. *Phys. Rev. Lett.* **2009**, *103*, 030603. [CrossRef]
52. Ceriotti, M.; Bussi, G.; Parrinello, M. Colored-noise thermostats 'ala carte. *J. Chem. Theory Comput.* **2010**, *6*, 1170. [CrossRef]
53. Crespo-Otero, R.; Barbatti, M. Spectrum simulation and decomposition with nuclear ensemble: Formal derivation and application to benzene, furan and 2-phenylfuran. *Theor. Chem. Accounts* **2012**, *131*, 1. [CrossRef]
54. Prlj, A.; Marsili, E.; Hutton, L.; Hollas, D.; Shchepanovska, D.; Glowacki, D.R.; Slavıcek, P.; Curchod, B.F. Calculating photoabsorption cross-sections for atmospheric volatile organic compounds. *ACS Earth Space Chem.* **2022**, *6*, 207. [CrossRef] [PubMed]

55. Sala, F.D.; Rousseau, R.; Görling, A.; Marx, D. Quantum and thermal fluctuation effects on the photoabsorption spectra of clusters. *Phys. Rev. Lett.* **2004**, *92*, 183401. [CrossRef] [PubMed]
56. Lee, S.Y.; Brown, R.C.; Heller, E.J. Multidimensional reflection approximation: Application to the photodissociation of polyatomics. *J. Phys. Chem.* **1983**, *87*, 2045. [CrossRef]
57. Lee, S.Y. Semiclassical theory of radiation interacting with a molecule. *J. Chem. Phys.* **1998**, *76*, 3064. [CrossRef]
58. Couto, P.C.D.; Hollas, D.; Slavıcek, P. On the performance of optimally tuned rangeseparated hybrid functionals for X-ray absorption modeling. *J. Chem. Theory Comput.* **2015**, *11*, 3234. [CrossRef]
59. Zeng, W.; Gong, S.; Zhong, C.; Yang, C. Prediction of oscillator strength and transition dipole moments with the nuclear ensemble approach for thermally activated delayed fluorescence emitters. *J. Phys. Chem.* **2019**, *123*, 10081. [CrossRef]
60. Oncak, M.; Sistık, L.; Slavıcek, P. Can theory quantitatively model stratospheric photolysis? ab initio estimate of absolute absorption cross sections of cloocl. *J. Chem. Phys.* **2010**, *133*, 174303. [CrossRef]
61. Slavıcek, P.; Oncak, M.; Hollas, D.; Svoboda, O. Abin, version 1.0. Available online: https://github.com/PHOTOX/ABIN (accessed on 16 July 2023).
62. Seritan, S.; Bannwarth, C.; Fales, B.S.; Hohenstein, E.G.; Isborn, C.M.; Kokkila- Schumacher, S.I.; Li, X.; Liu, F.; Luehr, N.; Snyder, J.W.; et al. Terachem: A graphical processing unit-accelerated electronic structure package for large-scale ab initio molecular dynamics. *Wiley Interdiscip. Comput. Mol. Sci.* **2021**, *11*, e1494. [CrossRef]
63. Ufimtsev, I.S.; Mart´ınez, T.J. Quantum chemistry on graphical processing units. 1. strategies for two-electron integral evaluation. *J. Chem. Theory Comput.* **2008**, *4*, 222 [CrossRef]
64. Ufimtsev, I.S.; Martinez, T.J. Quantum chemistry on graphical processing units. 3. analytical energy gradients, geometry optimization, and first principles molecular dynamics. *J. Chem. Theory Comput.* **2009**, *5*, 2619. [CrossRef]
65. Ufimtsev, I.S.; Martinez, T.J. Quantum chemistry on graphical processing units. 2. direct self-consistent-field implementation. *J. Chem. Theory Comput.* **2009**, *5*, 1004 [CrossRef] [PubMed]
66. George, S.D.; Petrenko, T.; Neese, F. Time-dependent density functional calculations of ligand K-edge X-ray absorption spectra. *Inorganica Chim. Acta* **2008**, *361*, 965. [CrossRef]
67. Stener, M.; Fronzoni, G.; de Simone, M. Time dependent density functional theory of core electrons excitations. *Chem. Phys. Lett.* **2003**, *373*, 115. [CrossRef]
68. Krylov, A.I. Equation-of-motion coupled-cluster methods for open-shell and electronically excited species: The hitchhiker's guide to fock space. *Annu. Rev. Phys. Chem.* **2008**, *59*, 433. [CrossRef] [PubMed]
69. Fransson, T.; Brumboiu, I.E.; Vidal, M.L.; Norman, P.; Coriani, S.; Dreuw, A. Xaboom: An X-ray absorption benchmark of organic molecules based on carbon, nitrogen, and oxygen 1s $\rightarrow \pi^*$ transitions. *J. Chem. Theory Comput.* **2021**, *17*, 1618. [CrossRef] [PubMed]

Disclaimer/Publisher's Note: The statements, opinions and data contained in all publications are solely those of the individual author(s) and contributor(s) and not of MDPI and/or the editor(s). MDPI and/or the editor(s) disclaim responsibility for any injury to people or property resulting from any ideas, methods, instructions or products referred to in the content.